Intense shear band plasticity in metallic glass as revealed by a diametral compression test

C. Bernard, S. Hin, Ludovic Charleux, Émile Roux, Y. Yokoyama, Alexandre Tanguy, V. Keryvin

Version of Record: https://www.sciencedirect.com/science/article/pii/S092150932201913X
Manuscript_ece41434dd2a70b23ab4a1f9acecf10f

Intense shear band plasticity in metallic glass as revealed by a diametral compression test

C. Bernard[a,*], S. Hin[a], L. Charleux[b], E. Roux[b], Y. Yokoyama[c], A. Tanguy[d], V. Keryvin[a]

[a]*Univ. Bretagne Sud, UMR CNRS 6027, IRDL, F-56321 Lorient, France*
[b]*University Savoie Mont Blanc, EA 4114, SYMME, F-74000, Annecy, France*
[c]*Laboratory for Advanced Materials, Institute for Materials Research, Tohoku University, Katahira 2-1-1 Aoba-ku Sendai City, Miyagi Prefecture 980-8577, Japan*
[d]*Laboratoire de Mécanique des Solides, École Polytechnique, UMR CNRS 7649, Institut Polytechnique de Paris, France*

Abstract

Shear band initiation, development and mutual interaction are studied in a $Zr_{55}Cu_{30}Al_{10}Ni_5$ metallic glass by means of an innovative experimental technique associating diametral compression test (or Brazilian test), scanning electron microscopy and digital image correlation analysis. The intense strain occurring in shear bands and the deformation map of their overall pattern are both estimated with a high resolution ($\sim$ 5 μm/pixel), offering a better understanding of the phenomenon. Finite element simulations based on a new and original plasticity model, the compartmentalized model, makes it possible to reproduce the shear band development observed experimentally, as well as the interlocking mechanism occurring between the shear bands.

Keywords: Plasticity; Bulk metallic glass; Shear bands; Digital image correlation; Brazilian test

*Corresponding author: cedric.bernard@univ-ubs.fr

1. Introduction

Bulk metallic glasses (BMGs) are known to have many advantages in terms of mechanical properties. For example, they exhibit high levels of strength, yield strain, stored elastic energy and hardness [1, 2]. However, unlike their crystalline counterparts, they are apparently brittle at room temperature in uniaxial loading, which represents a major obstacle to their industrialization. Shear bands (SBs), and more particularly the way they initiate and propagate, are the key parameter to improve their plastic deformation [3]. Given that the worst case scenario is that the major part of the deformation of the specimen is concentrated in a unique shear band [4, 5], researchers have tried to improve the ductility by preventing such a scenario. Thus, efforts have been made to develop a more diffuse SB pattern in the samples during their deformation by favoring the initiation of SBs in numerous sites or favoring their branching; but also by deviating, impeding or even blocking the propagation of the existing SB. Many attempts have been made during the last decades and positive results have been achieved. The main strategy is to make the glass more heterogeneous or to taylor the specimen geometry to induce a complex stress field [6] in the specimen and ease the nucleation of multiple SBs. To reach this goal, a second phase (crystal [7, 8], pore [9] or other types of inclusions [10, 11]) was introduced in the matrix, or the sample surfaces were modified by local plastic deformations, e.g. via imprinting [12], by creating a micro-pits array [13], or by shot peening [14]. Using tilted or notched samples is another means to induce high gradients in the local stress distribution [6, 15]. Introducing primary SBs into the matrix by a first loading cycle, via cold rolling [16] or via uniaxial compression [17, 18] for instance, also gave good results in terms of plasticity for the subsequent loadings. Another way

to induce and investigate large macroscopic deformation in BMGs is to generate a constrained plasticity in the specimen by means of specific tests. Among these, compression tests on specimens with a low sample aspect ratio [4] or indentation tests [19, 20] are well known. In this paper, a less conventional test, the diametral compression test or Brazilian test [21] which is mainly used on brittle materials such as rocks or concrete, is carried out for the following reasons. Unlike indentation tests, the constrained plasticity zone induced by the Brazilian test is large and can be directly observed from its two free plane surfaces throughout the whole test. Moreover, since these free surfaces are plane, the measurement of the displacement field with the digital image correlation (DIC) technique is easier than for classical compression tests whose free surfaces are curved, as reported in Wu *et al.* [22]. Finally, the maximum macroscopic strain achievable with this test is higher than with that of classic compression tests. The measurement of the strain field of a BMG Brazilian disk with the DIC technique has already been performed in a previous study [23] on bulk metallic glass. But the resolution of the strain map obtained was too low ($\sim$ 250 µm /pixel) to analyze the localization of the strain due to particular test conditions: the pattern sprayed on the sample was coarse and the camera was far from the sample.

In the present paper, we propose an innovative measurement technique combining Brazilian tests, scanning electron microscopy (SEM) and the DIC technique to measure the strain field under loading with a resolution of up to 5 µm/pixel. Thus, finer analysis of the deformation is made possible and the evolution of shear bands, in which the flow is concentrated, can be both observed and characterized. Due to this higher resolution, a more accurate assessment of the high strains developing in the shear bands is proposed. Fi-

nally, experimental results are quantitatively and qualitatively compared to a finite element simulation based on a simple but original model: the compartmentalized model.

2. Materials and experimental methods

2.1. Materials and specimens

The specimens were prepared from a Zr-based bulk metallic glass with a quaternary eutectic composition $Zr_{55}Cu_{30}Al_{10}Ni_5$ (at%) The processing sequence, which was totally automated, as described in [24], consisted of three steps: (i) weighing the raw metals to achieve the target stoichiometry, (ii) pre-alloying and then alloying in an inert argon atmosphere by remelting several times and, (iii) casting into rod-shaped specimens by tilt casting in an arc furnace. The oxygen concentration of the bulk amorphous alloys, about 500 ppm, was measured using a fusion in helium gas-infrared absorption method. Table 1 recalls the main mechanical properties of the material, measured in previous studies [25, 26]. No crystalline defects were observed in the glassy matrix.

Mass density ρ (g.cm^{-3})	Young's modulus E (GPa)	Shear modulus μ (GPa)	Bulk modulus B (GPa)	Poisson's ratio, ν (-)	Tensile yield strength, σ_y (GPa)	Compression yield strength, σ_{yc} (GPa)
6.83 ±0.01	84.4 ±0.8	30.9 ±0.3	103.5 ±1.16	0.364 ±0.007	1.6	1.8

Table 1. *Main mechanical properties of $Zr_{55}Cu_{30}Al_{10}Ni_5$ (at%) metallic glass [25, 26]*

The rough curved surface of 3 as-cast rods, named A, B and C, was shaped into 3 proper cylindrical geometries by means of a cylindrical grinding machine with the nominal diameters of 2.8 mm, 2.47 mm and 2.25 mm, respectively. These long and smooth cylinders were then cut into smaller ones using a water lubricated diamond disk and the plane surfaces created during this

operation were then mirror polished. The samples were divided into three batches named A, B and C depending on the rod they were cut from. In other words, the samples in a same batch have the same diameter. The resulting geometry is presented in Figure 1 and the specimen dimensions are summarized in Table 2.

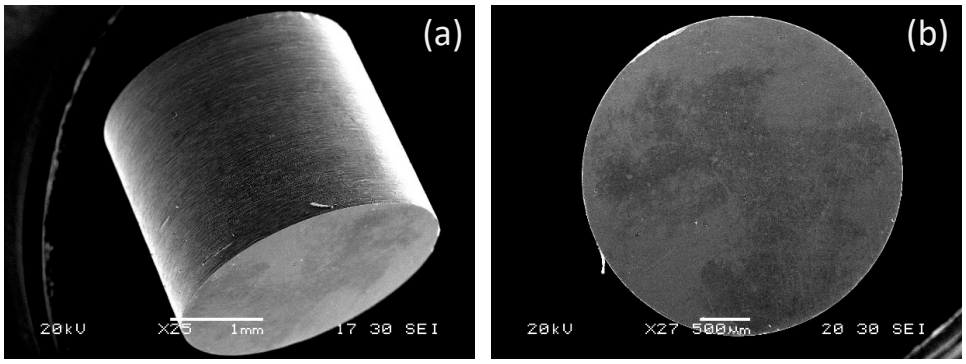

Figure 1. *Cylindrical sample of metallic glass $Zr_{55}Cu_{30}Al_{10}Ni_5$ (at%) imaged by SEM. The two plane surfaces were polished and the curved surface was shaped by means of a cylindrical grinding machine. (a) Tilted view of the sample, (b) Detailed view of a plane surface.*

Batch	Specimen name	Diameter D (mm)	Thickness e (mm)	SEM observations
A	A1	2.80 ± 0.02	3.13 ± 0.02	ex-situ
	A2		2.96 ± 0.02	
B	B1	2.47 ± 0.02	2.51 ± 0.02	ex-situ
	B2			
	B3			
C	C1	2.25 ± 0.02	2.46 ± 0.02	in-situ
	C2			

Table 2. *Dimensions and condition of observation of the specimens.*

For batches A and B, Brazilian tests were performed using an Instron 5567 universal testing machine equipped with two parallel compression platens (Figure 2-a). The cylindrical specimen was placed between the platens with

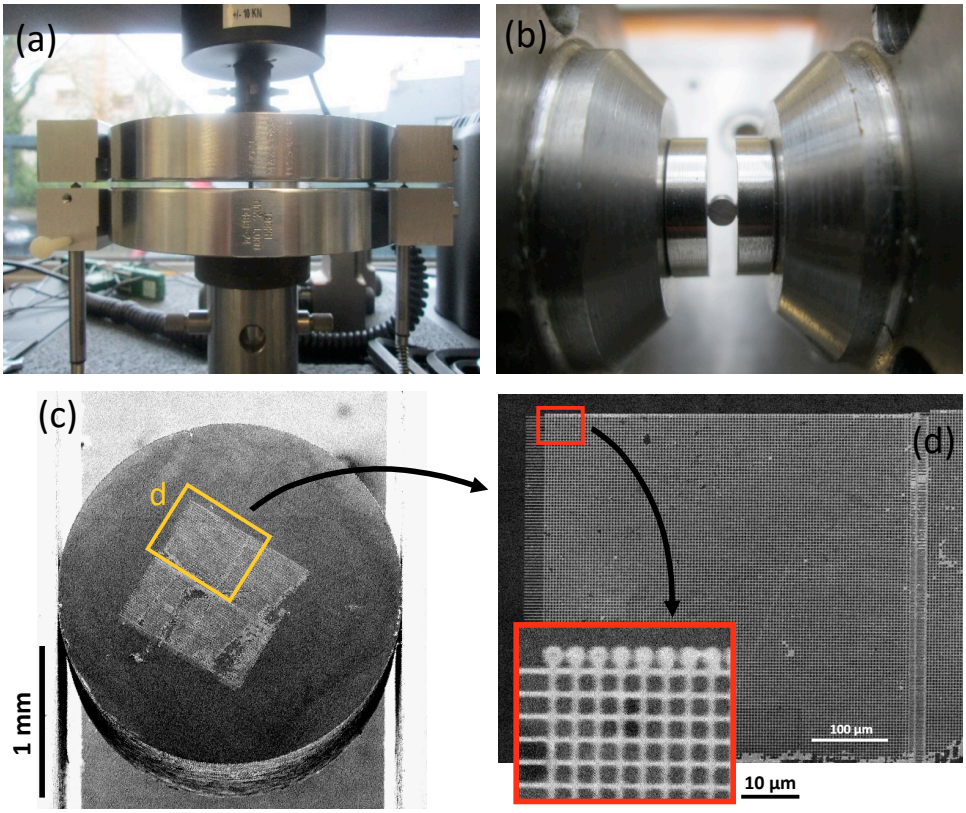

Figure 2. *Experimental setup: (a) Standard compression testing machine with LVDT displacement sensors, (b) compression testing machine placed in an SEM. Overall (c) and detailed (d) views of the gold micro-grid deposited on the specimen C1.*

its revolution axis normal to the loading direction. Thus, the contact between the sample and the platens occurs along two diametrically opposed generatrices, as required by the Brazilan test protocol. The relative displacement of the platens, δ, was measured by means of two Linear Variable Differential Transducers (LVDTs) mounted on the moving platen. Brazilian specimens from batches A and B were subjected to several cycles of loading and unloading with a peak force P_{max} increasing gradually at each cycle up to 10 kN. For the first specimen of each batch, i.e. A1 and B1, the test was interrupted between each cycle. The specimen was extracted from the set-up, put in a scanning electron microscope (SEM, JEOL-JSM-6460LV) to be imaged and replaced between the platens to perform the next cycle. For these interrupted tests, crosshead loading and unloading velocities were respectively: 0.002 and 0.01 mm/s. For the other specimens, the test was not interrupted, crosshead loading and unloading velocities were both 0.004 mm/s and SEM observations were performed only at the end of the test.

Brazilian specimens from batch C were dedicated to full-field displacement measurement by the digital image correlation (DIC) technique, which is why one plane surface of each specimen was marked. A gold micro-grid with a pitch of 4 μm and a line width of $\sim$ 0.8 μm was printed over a 500 × 500 μm^2 area using electron beam lithography [27]. An overall view and a detailed view of such a grid is illustrated by micrography in Figures 2-c and -d, respectively. It should be noted that, due to the lack of reliability of this deposition technique, only a part of the zone covered by the grid was finally usable on specimens C1 and C2. Figures 2-c and -d clearly show that only a quarter of the grid (frame d) was properly deposited on the sample C1. For sample C2, only the central area was usable. Next, the specimens experienced diametral

compression by means of a compression machine (a prototype developed by Kammrath & Weiss GmbH, see Figure 2-b) mounted inside the chamber of an SEM (Philips XL40). Only one cycle of loading and unloading was performed up to $P_{max} = 10$ kN at the velocity $\dot{\delta}$ =0.002 mm/s, with δ being the relative displacement of the platens. During the loading stage, the crosshead displacement was stopped every 0.1 mm for a few minutes to image the marked plane surface of the specimen by SEM. Since the maximum displacement of the moving platen was about 1.3 mm, 14 images were recorded for each specimen. At each stage, one overall picture of the specimen and one magnified picture of the grid area were taken by SEM (8-bit gray levels, 4096×4096 pixels). The correlation process was applied to the last ones with the software CorrelManuV [28]. The subsets, with a size of 25×25 pixels, were centered on the grid intersections for all the images. The relative displacement of the platens δ was directly measured here on the overall picture of the sample taken by SEM, i.e. the distance from one edge in contact with a platen to the other one. This relative displacement of the platens is much more accurate than the crosshead displacement of the set-up, because it is not at all affected by its compliance. It should be noted that measurement of δ on batches A and B is affected by the stiffness of the machine: the platens, on which LVDTs are mounted, experience elastic deformation during loading. As a consequence, all the experimental curves from batch C involving δ cannot be compared to those from batches A and B.

Compared to a more conventional technique such as random spray paintings, gold micro-grid deposition does not totally cover the observed surface, and thus allows direct observation of interesting phenomena such as shear bands or crack development. However, the regularity of the grid pattern asso-

ciated with the high localization of plastic deformation — the sliding distance in the SB can be several times the grid step — prevents a totally automatic correlation process by the software. For this reason, some reference points had to be found by the user and placed manually by selecting a pixel on the image directly [29] at each stage of the deformation.

Finally, the components of the objective Green-Lagrange strain tensor, $\underline{\underline{E}}$, were computed from the displacement field $\vec{U}$:

$$\underline{\underline{E}} = \frac{1}{2}\left(\underline{\underline{F}}^T.\underline{\underline{F}} - \underline{\underline{I}}\right), \text{ with } \underline{\underline{F}} = \nabla\vec{U} \tag{1}$$

where $\underline{\underline{I}}$ is the identity tensor of order two and $\underline{\underline{F}}$ denotes the deformation gradient. It should be noted that the DIC technique can only measure the displacement in the plane of the grid, defined as $(\vec{x}, \vec{y})$ with $\vec{x}$ being the loading direction. Consequently, since the out-of-plane displacement component U_z is unknown, the only three strain tensor components that could actually be calculated were: E_{xx}, E_{yy} and E_{xy}. For the same reason, the von Mises equivalent strain can not be determined either. However, if the strain tensor is supposed to be axisymmetric locally with two of its principal strains in the $(\vec{x}, \vec{y})$ plane, then E_{zz} becomes computable and, by extension, this is likewise for the Green-Lagrange von Mises equivalent strain E_{eq}. According to this approach, the out-of-plane strain component E_{zz} must be taken as being equal to the lower in-plane principal strain. For more details about the calculation of $\underline{\underline{F}}$ and E_{eq} in this context, see Allais *et al.* [27] for example.

3. Results

3.1. Qualitative results

First, the plastic behavior of BMG can be investigated by analyzing its response at a macroscopic scale. Figure 3 shows the normalized load vs normalized displacement response for the specimens of the batches A and B. Experimental data are normalized by the thickness and the diameter so as not to be affected by the variability in the specimen dimensions. The same experimental data reported in a previous study [23] were also added for the sake of comparison. Curves in Figure 3 illustrate the good reproducibility observed in the macroscopic mechanical response for all the specimens of batches A, B and even the specimens from Brest *et al.* [23] that exhibit particularly high diameters (8 mm) and thicknesses (6 and 15 mm). It must be noted that, for this previous work [23], platen displacement was also measured by two LVDTs mounted on the moving platen, which allows a direct comparison with experimental data from batches A and B.

Note that the elastic unloading and loading parts of the curve A1 do not perfectly overlap. This lack of accuracy can be easily explained by test conditions: specimen A1 was removed from the platens and then replaced between them at each stage to be imaged by SEM.

The evolution of the pattern created by the SB emerging from the plane faces of the specimen also shows good reproducibility. These characteristic patterns, observed during the Brazilian tests, are schematically represented in the lower part of Figure 3. Figure 4 shows an example of this pattern on the sample A1 imaged by SEM at the end of the test (after being loaded up to $P = 10$ kN). Similar patterns can also be observed in Figures 5-a and -e, which present two samples from batch C imaged during in-situ tests (the samples

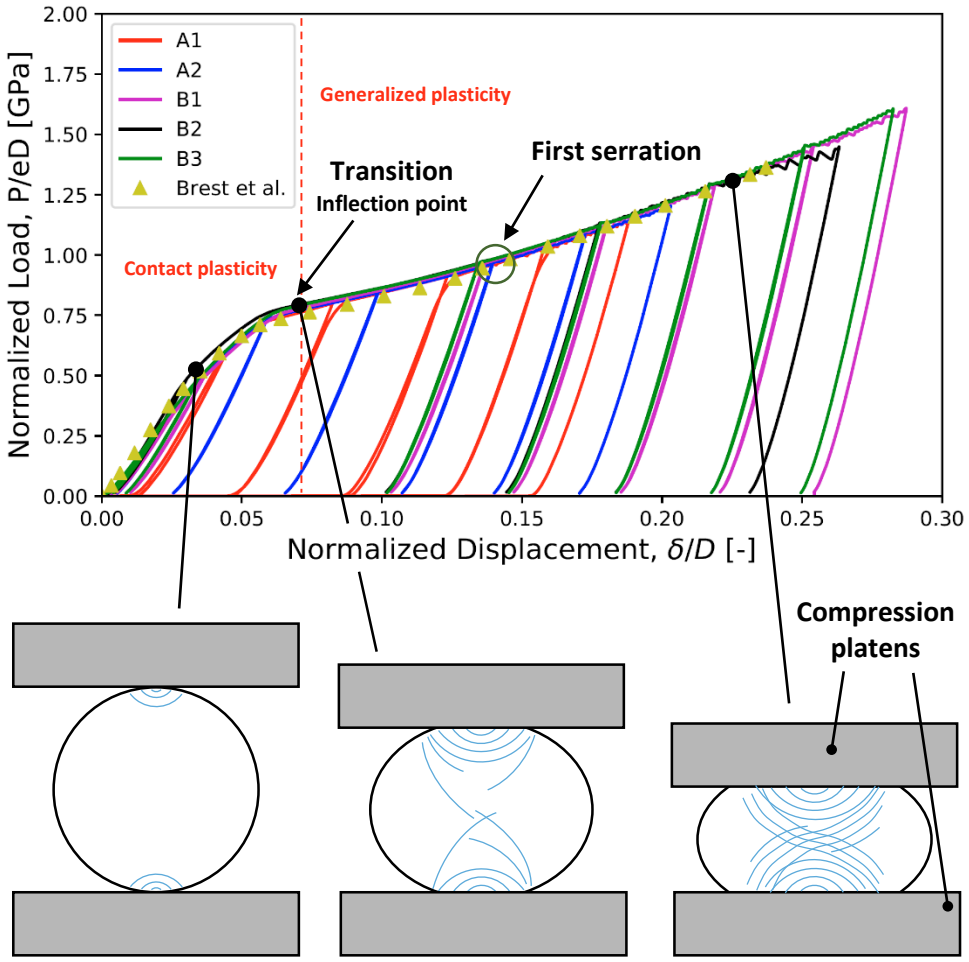

Figure 3. *Upper part: Normalized load vs normalized displacement curve for the specimens from batches A and B along with results from Brest et al. [23]. Lower part: typical patterns observed on the surface of the specimen during the test.*

from batch C, contrary to A and B, were loaded during the scanning process). For the latter, magnified views of the deformed grid — micrographs of Figures 5-b to -d and -f to -h — give a better understanding of SB development.

According to the curves in Figure 3, two stages can be distinguished during the test: the first part of the curve is non-linear with a high slope, and the second part is almost linear and rises less quickly. These will be called contact plasticity and generalized plasticity stages, respectively.

In the first stage, two plastic zones are confined in the close vicinity of the contacts between the platens and the sample while the rest of the sample is free of plasticity. A similar phenomenon has already been observed underneath an indenter in previous studies [25, 30]. As the force increases, the SBs grow toward the center of the specimen following arc-shaped paths. Their density increases in parallel. The sudden decrease of the loading slope corresponds to the moment when the two plastic zones meet in the center of the specimen. This observation has been reported by Brest *et al.* [23]. From this point on, the contact plasticity stage ends and the generalized plasticity stage begins.

During this second stage, the plasticity zone crosses the entire specimen and forms a kind of plastic hinge similar those usually encountered, for example, in beams loaded in bending. This explains why the slope of the curve decreases quickly. However, the non-plasticized region of the specimen is large enough to keep a non-zero slope. Thus, although the load increases, the plastic zone stops expanding, while both density and the shear strain level of the SBs keep increasing. This phenomenon is illustrated by the numerous discontinuities that appear in the grid pattern applied to batch C specimens. Figure 5-f, for instance, shows the high SB density in the center of specimen C2,

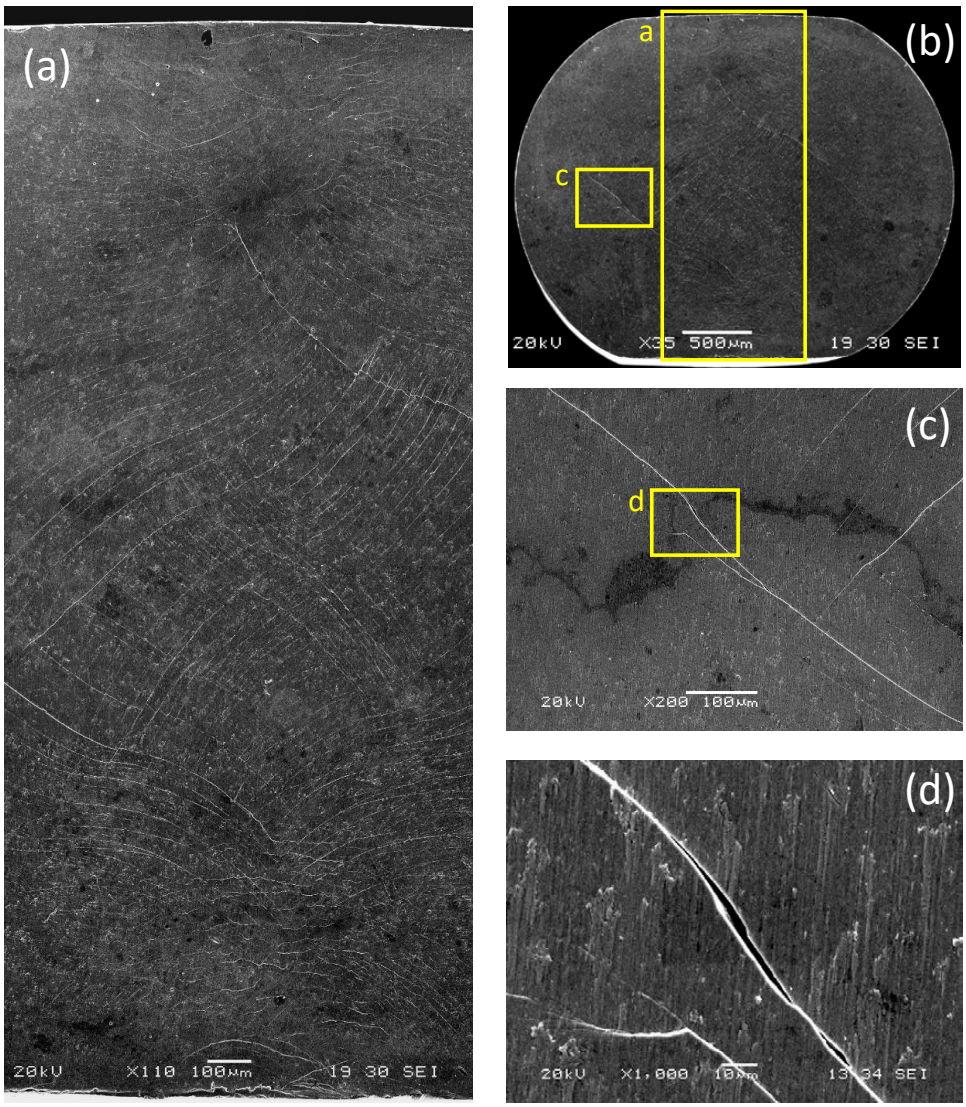

Figure 4. *SEM observations of a plane face of sample A1 loaded at $P = 10$kN, i.e. $\delta/D \gtrsim 0.2$. (a) Central part of the sample between the two contact zones. (b) Overall view of the sample. (c and d) Views of a crack stemming from a shear band. Images a), c) and d) are localized by the 3 yellow rectangles. Loading direction is vertical.*

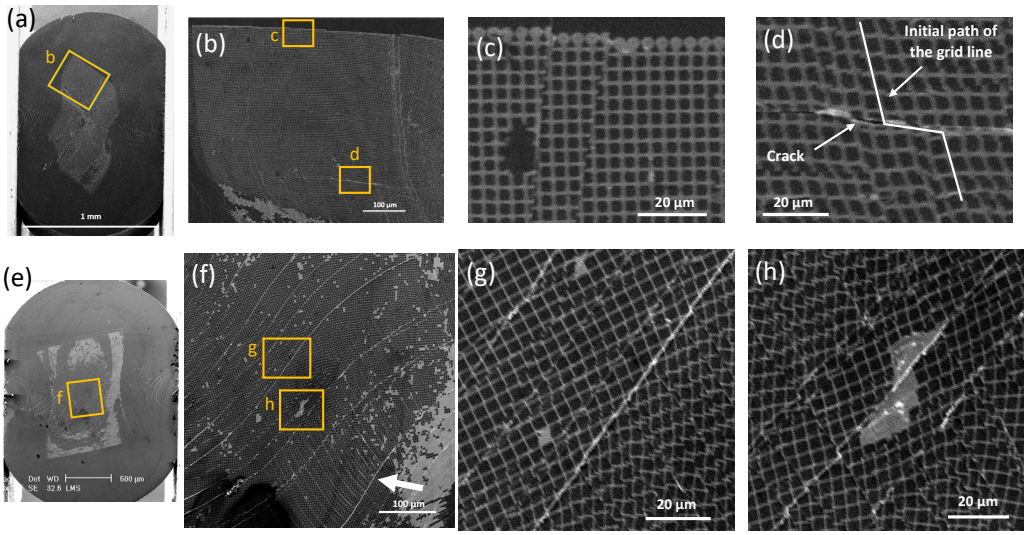

Figure 5. *(a) and (e): Overall views of the specimens C1 and C2, respectively, for a normalized displacement of $\delta/D = 0.24$ and 0.19, respectively. (b) Magnification of the top corner of the correlation grid. (c) Zone with two vertical SBs slipping along about half a grid step. (d) Zone close to the center with a horizontal SB slipping along about 3 grid steps. This SB has clearly degenerated into a crack (f) Magnification of the center of the correlation zone. The white arrow indicates a major primary SB blocking many secondary SBs. (g) and (h): Magnification of two areas highlighting the blocking process addressed in (f). Loading direction is horizontal.*

and the magnified views of Figures 5-g and -h reveal different rigid domains slipping intensively against each other along these SBs.

SEM images also show the transformation of some SBs into cracks as shown in Figures 4-c and -d, reflecting the onset of the damage in the material at high relative displacement, i.e. $\delta/D \gtrsim 0.2$. The occurrence of the first serration of the curve seems to coincide with the first SB that completely crosses the sample from the upper contact surface to the lower one. The orientation of the SB at the center of the specimen is favored along two directions, $+45^\circ$ and -45° with respect to the loading direction. Thus, the pattern observed in the central area is a network of SBs crossing each other like in the "χ" symbol. This pattern is close to the one reported in Ref. [23] which was obtained both experimentally, but with a much lower resolution, and numerically. It should be noted that, for several samples, most of the SBs follow only one of these directions. This phenomenon is probably due to a small defect in the cylindrical geometry of the sample or in the parallelism of the platens. In a first approach, the intensity of the shearing in the bands can be estimated by a direct observation of the grid deposited on the specimen. Figures 5-a to -d show the grid of the sample C1 in a deformed configuration accounting for a normalized displacement of $\delta/D = 0.24$. The magnified view of two different areas clearly shows the intensity of the shearing in the SB. Figure 5-c presents slips along two vertical SBs on about half of a grid step (~ 2 µm). Figure 5-d, which magnifies an area closer to the center of the same specimen, a slip of 3-grid-step-long (~ 12 µm) can be observed along a horizontal SB that has degenerated into a crack. It should be noted that the SBs are so thin — down to 20 nm according to [3, 31] for instance — that even in the most magnified SEM image (Figure 5-e) their thickness is not visible.

Figures 5-f to -h show that the center of the sample C2, for a normalized displacement of $\delta/D = 0.19$, is crossed by SBs oriented along two favored and symmetric directions, that will be called \ and /. The SBs inclined along the \ direction seem much more numerous than the ones along the / direction and particularly in certain areas, in the lower right part of Figure 5-g and h and in the upper left part of Figure 5-h, for instance.

It is noteworthy that many secondary SBs are blocked by a larger SB oriented in the other direction, as illustrated in Figure 5-f. In this micrograph the white arrow indicates a major SB, oriented along the / direction, which blocks a lot of secondary SBs oriented along the \ direction. These blocked secondary SBs show a much higher density.

3.2. Quantitative results

Figures 6 and 7 show the strain maps of the correlation zone of the specimens C1 and C2 for the 14 successive stages of the Brazilian test and the corresponding load vs displacement curves. Note that in the last part of the test on specimen C2, the grid was so stretched and distorted that the image could not be exploited by DIC. These last 3 stages are symbolized by black crosses on the curve of Figure 7-a. The reason why C1 did not experience the same problem is probably that its correlation area was less close to the center of the sample, and consequently the strain level was less intense and less localized. For each specimen, the maps of the first 4 stages do not show any particular pattern. The dark blue color visible on these whole maps evidences that strain is both uniform and low ($\delta/D < 0.04$), suggesting that the deformation is both elastic and not localized in these parts of the specimens.

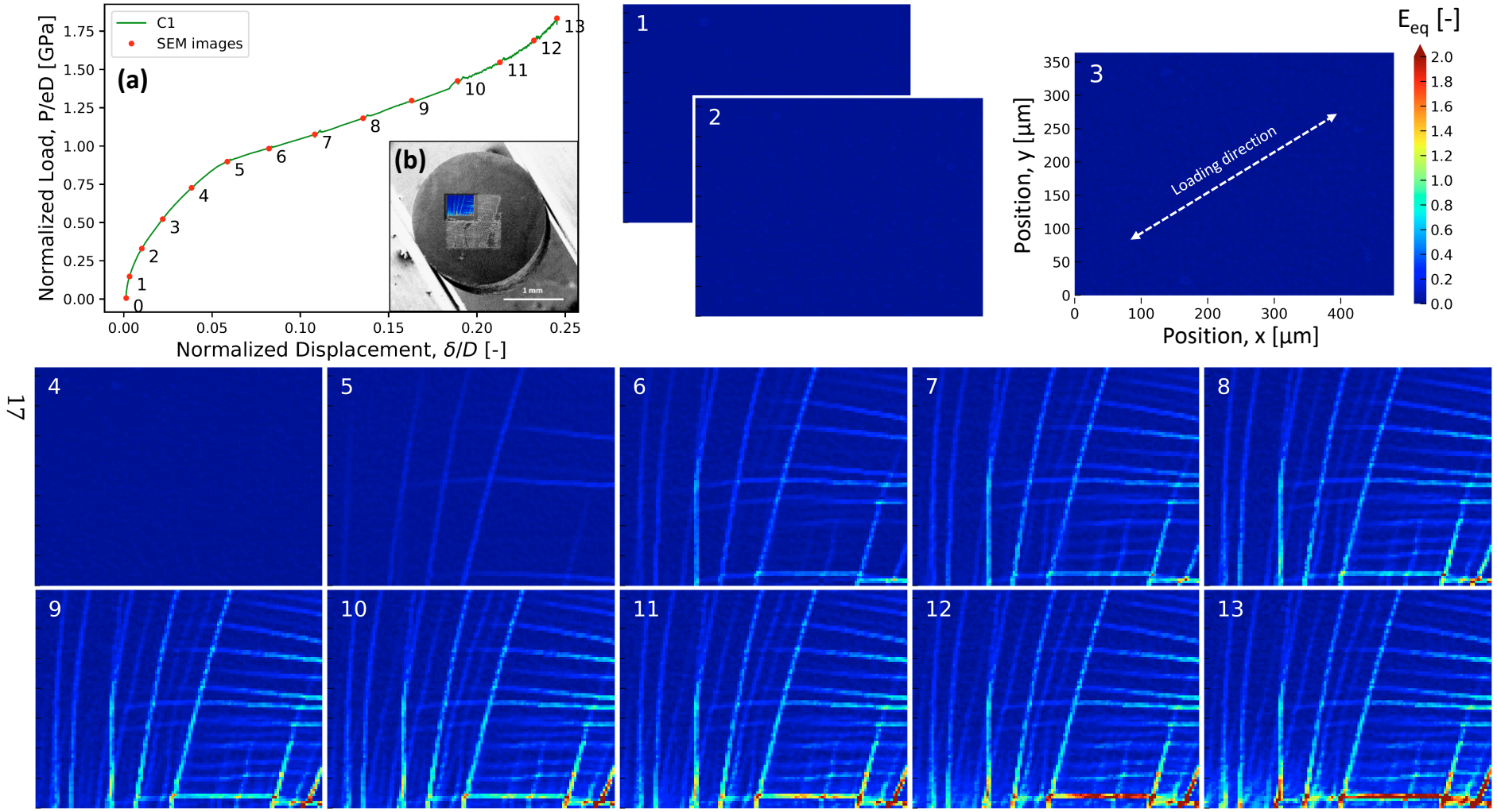

Figure 6. *(a): Normalized load vs normalized displacement curve of the Brazilian test on sample C1. (b): A deformation map superimposed on an SEM image of the sample in its initial configuration. The von Mises equivalent deformation, E_{eq}, maps of the correlation zone are displayed at several stages (symbolized by red dots and labels on the curve). Maps are all represented in the initial configuration and the values are truncated at $E_{eq} = 2.0$.*

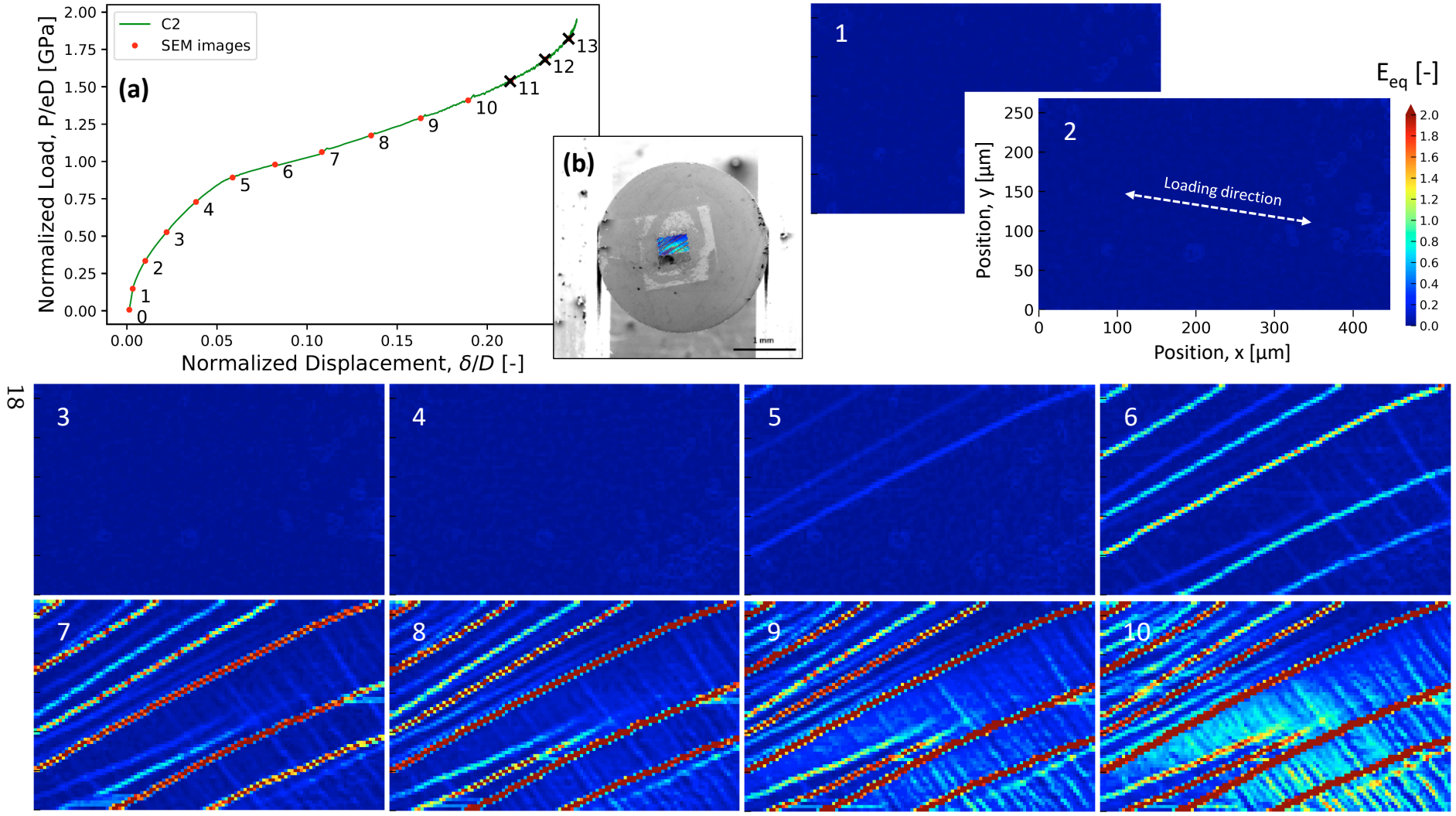

Figure 7. *(a): Normalized load vs normalized displacement curve of the Brazilian test on sample C2. (b): A deformation map superimposed on an SEM image of the sample in its initial configuration. The von Mises equivalent deformation, E_{eq}, maps of the correlation zone are displayed at several stages (symbolized by red dots and labels on the curve). Maps are all represented in the initial configuration and the values are truncated at $E_{eq} = 2.0$. For the 3 last SEM images (symbolized by the black crosses), the grid was too stretched and distorted to be exploited by DIC.*

For each specimen, the first signs of strain localization visible in the correlation window appear at stage 5 ($\delta/D = 0.06$), i.e. close to the inflection point of the curve. This strengthens the idea that the transition between the two behaviors highlighted by the curve P vs δ occurs when the two opposite plastic zones meet at the center of the specimen.

It is noteworthy that two displacements can be investigated during this test, and each of them has a drawback. On the one hand, the crosshead displacement, λ, which is continuously recorded by the compression set-up and which can capture the serrated nature of the curve, is highly affected by machine compliance. On the other hand, the relative displacement of the platens, δ, which should be more appropriate, because it is the displacement actually experienced by the contact surfaces of the sample. δ can be measured only at the 14 stages during which the displacement is stopped to image the sample, because it is directly measured on the SEM pictures of the overall sample, such as those presented in Figures 5-a and -e. However, by means of these 14 values, the relationship between λ and δ was approached by a 4^{th} degree polynomial function. Finally, by means of this function, the original experimental P vs λ continuous curve was transformed into a P vs δ continuous curve. These curves are presented in Figures 6 and 7 for specimens C1 and C2, respectively.

4. Discussion

4.1. Ductile behavior and strain localization

The experiments detailed above show that the Brazilian test is particularly suitable for studying the plasticity of BMGs. The set-up developed for

this study offers the innovative opportunity to conveniently observe the stable development of shear bands during the test, because the plane face of the specimen can be directly imaged during the test. Moreover, very large plastic deformations can be achieved because the plasticity stays confined in the central part of the sample. Both ex-situ and in-situ tests show that the specimens experienced an intense and steady plastic deformation at macroscopic scale. Figure 3 shows that the tests on $Zr_{55}Cu_{30}Al_{10}Ni_5$ metallic glass are highly reproducible both from a macroscopic point of view (normalized load vs. normalized displacement curves) and with respect to the patterns formed by the SBs on the sample surface. This last idea is reinforced by Figure 8 which presents the deformation map of C1 and C2 in their respective correlation zones, but placed in the same global coordinate for the same global deformation level ($\delta/D = 0.19$). The two maps overlap and are very similar in terms of density, pattern and strain level. It is noteworthy that, no significant impact of the different loading and unloading velocities on the material response has been evidenced.

The pattern revealed by SEM observations (in Figures 5 and 4) gives information about some mechanisms behind the high plasticity and the steadiness of the deformation. On the one hand, as has already been shown in the case of indentation [32, 25, 30] or compression [33, 6] tests, the propagation of SBs generated by the high stresses below contact is limited by the more moderate stresses in the surrounding bulk. In this case, as in the case of indentation, the first SBs initiated in the contact zone cannot propagate to the free edges, thus preventing premature sample failure. Finally, the SBs intersecting along two main directions in the central region of the specimen interfere with each other, which also increases the plasticity in the structure. Wang *et al.* [34] or

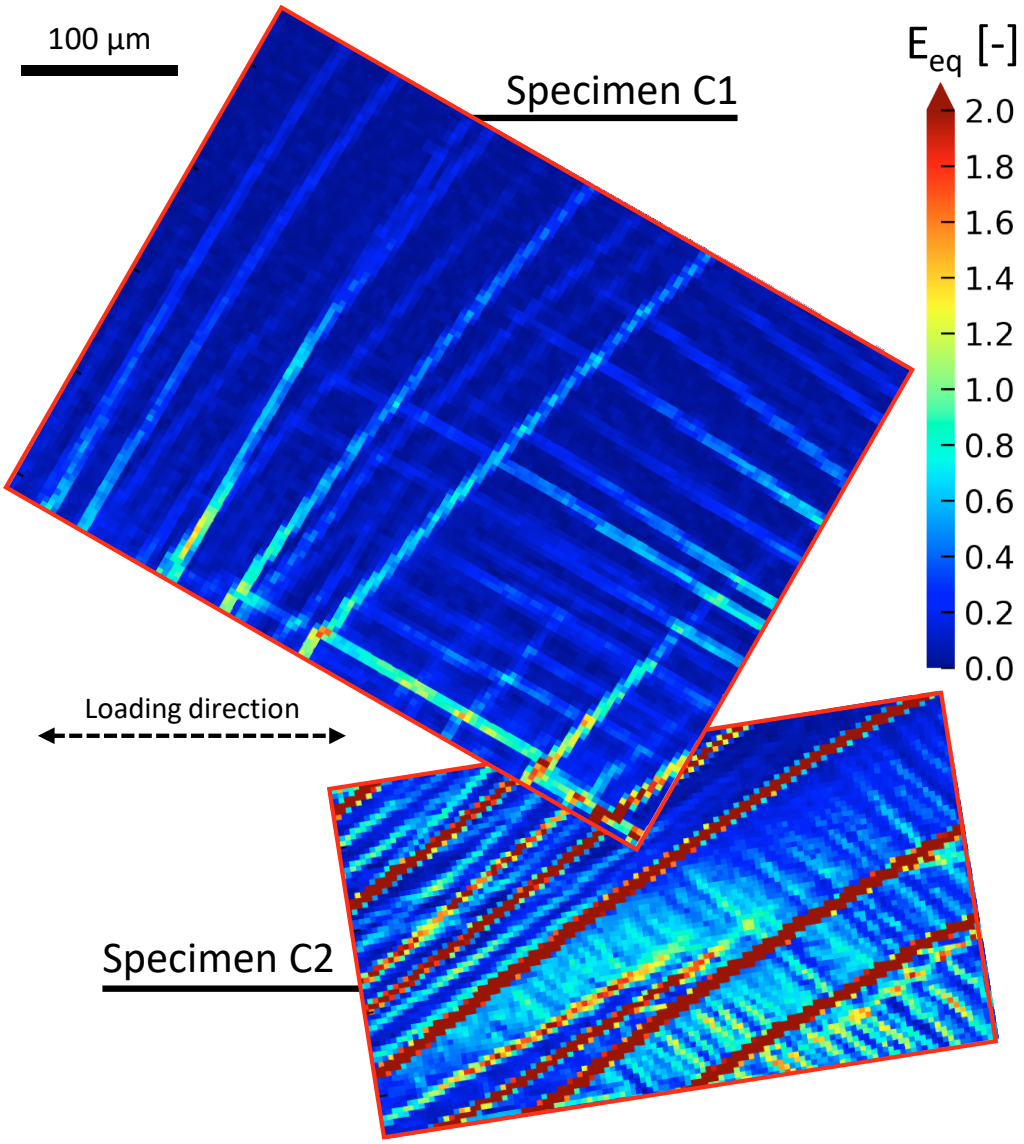

Figure 8. *Von Mises equivalent deformation maps of the correlation zone of each sample at the same stage of the test in the initial configuration and truncated at $E_{eq} = 2.0$. Once they are placed in a same global spatial coordinate, these two maps are clearly overlapping. The loading direction is horizontal.*

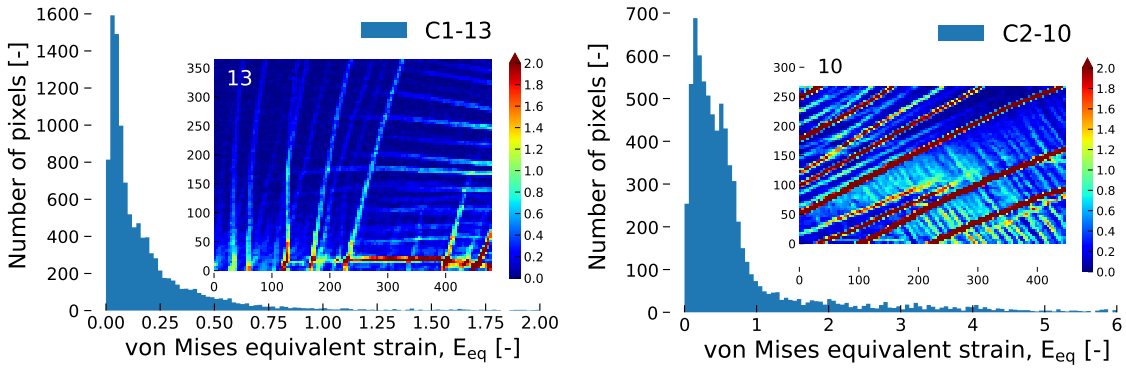

Figure 9. *Distribution of the von Mises equivalent strain level in samples C1 and C2 at the latest stage where their deformation map (truncated at $E_{eq} = 2.0$) was measured, i.e. stages 13 and 10 respectively. Deformation maps are truncated at $E_{eq} = 2.0$.*

Chen *et al.* [6] indicated that, in general, interaction between SBs is prone to increased ductility and greater plastic dissipation capacity. Mondal *et al.* [35] also linked the macroscopic ductility of BMGs in compression tests to the interaction of SBs occurring in the specimen. They also speculated that the mechanical interlocking of cracks resulting from the degeneration of SBs into cracks may play a key role in the ductility of BMGs. Another example, Zhao *et al.* [36] showed that symmetrical main SBs that intersect in a specimen under compression loading can considerably impede the rapid propagation of major SBs.

The strain maps obtained by the DIC technique have a resolution of only a few micrometers (cf. Figures 6 and 7) and offer an accurate means to quantitatively characterize SB behavior. Figure 9 presents the distribution of the von Mises equivalent strain E_{eq} in the correlation area at the stage for which specimens C1 and C2 are the most loaded (i.e. stages 13 and 10 respectively). Note that due to its position in the center of the sample, the C2 correlation area experiences higher deformations than that of C1. The distribution related to sample C2 reveals that the equivalent strain is above 2 in a non-negligible

part of the pixels, essentially localized in major SBs. It also gives the highest strain value in the C2 map: $E_{eq} \approx 6$. The intense shearing in the SBs, already revealed by the deformed grid in Figure 5 for instance, can explain these very high strain values. Such a tremendous deformation level in a BMG specimen during a test that allows a direct observation of steadily developing SBs, has not yet been reported in the literature, to our knowledge. Nekouie *et al.* [37], for instance, imaged via SEM and analyzed a deformed grid on the surface of a BMG specimen, but they did not use it to evaluate a deformation map. Wu *et al.* [22] also used DIC, with a similar resolution ($\sim$ 6 µm/pixel), to measure the strain field on the surface of the sample by means of a classical compression test. However, the treatment of their images was complicated by the curvature of the lateral surface observed, and the plasticity level achievable by this technique was very low (the maximum von Mises strain measured in SBs did not exceed ~ 0.06). It is noteworthy that, due to its very low thickness (less than 100 nm [3]), the accuracy of strain measured in an SB depends on the resolution of the strain map. For this reason, the maximum strain value measured in a previous study [23] was much lower, i.e. a logarithmic strain of only 0.2 for a similar normalized load, than the one in the present study, because the map resolution was only $\sim$ 250 µm/pixel. Also, to approach the real value, the pixel length of the correlation zone should be of the same order as the SB thickness. It is noteworthy that, due to the compressive nature of the Brazilian test, it may be expected that many cracks stay closed during the test (contrary to the crack in Figures 5-d and 4-d, which is open and clearly visible). Consequently, on the SEM images, and even more so on the DIC strain maps, it is difficult to distinguish cracks (involving decohesion and surface creation) from SBs (involving only plastic mechanisms). Since it is

impossible to detect if an SB has degenerated into a closed crack or not, the term SB must be understood in this paper as both shear bands and possible closed cracks.

4.2. Modeling the test using the Compartmentalized model

Previous studies — see Brest *et al.* [23] for example — succeeded in numerically reproducing these particular shear band patterns in BMGs. The models used were physically-based and complex, such as the Anand and Su elastic-viscoplastic model [38] for instance, and involved both pressure-sensitivity and plastically-dilatant behavior. The aim of this part is to approach the plasticity localization occurring in the sample as well as its macroscopic response using an original and much simpler constitutive model: the compartmentalized model. A compartmentalized model is a random heterogeneous finite element model in which the material properties of every element stem from those of a substructure called a compartment [39, 40]. In the model presented, each element is a compartment. Compartments are not designed to represent a specific physical structure of the material. Their only purpose is to introduce a controlled amount of heterogeneity in the model to produce specific effects on the macroscopic mechanical behavior. The implementation and detail description of the model can be found in [40]. Such heterogeneity is consistent with the free volume distribution in the material and more generally with the STZ activation process involved in BMG deformation, even if the scale of this physical phenomenon is much finer than the specimen mesh scale. The implementation of the compartmentalized model described in this section is made available by the authors (Python libraries: Compmod2 [41] and Argiope [42], full code example: Compdmod2 documentation [43].

The finite element simulations were carried out using the commercial implicit solver Abaqus/Standard (2019 version). A cross-section of the sample with the same diameter as C1 and C2 was modeled using the plane strain assumption (CPE4R Abaqus element). The mesh, containing 166,000 elements, was generated using the Gmsh Blossom-Quad algorithm [44] with a target element size of 5 μm. Thus, the mesh size was consistent with the size of the micro-grid deposited on the specimen and used to measure the strain field during the tests. Platens were modeled using analytic rigid bodies, with a low friction coefficient equal to 0.02. The lower platen was fixed, the upper one was moved down.

Each compartment was associated with a unique but very basic material: isotropic, linear elastic and J_2 perfectly plastic, where J_2 denotes the second invariant of the deviatoric stress tensor. Consequently, no hardening or softening was implemented in the material. Moreover, the elastic behavior of all compartments was set as homogeneous. Their Young's modulus had a fixed value of $E = 84.4$ GPa and their Poisson's ratio was $\nu = 0.364$ as in Table 1. Heterogeneity was introduced to the model through the yield strength σ_y. All compartments were defined in order to have a σ_y value following a uniform distribution over the range $[1800\text{ MPa} - 1900\text{ MPa}]$. Finally, a random mapping was used to associate each element with a unique compartment.

The choice to simulate a test with a specimen from batch C, rather than A or B, was motivated by the fact that the displacement δ is directly measured at the edges in contact with the platens, thanks to SEM images. Conversely, for tests with specimens from batches A or B, the compliance of the machine must be taken into account. Thus, the platens on which the LVDTs were mounted should have been modeled as elastic bodies.

Figure 10 shows the response curve of the simulation along with the experimental results from tests performed in-situ on specimens C1 and C2. Note that the computation did not exceed a normalized displacement of ~ 0.17, i.e. just after stage 8, because some elements experiencing too high a level of distortion stopped the computation. A good agreement between simulation and experimental normalized load vs normalized displacement curves can be observed up to $\delta/D \approx 0.17$, which tends to validate the compartmentalized model regarding the macroscopic response, at least for the beginning of the test. The two stages of the specimen deformation previously observed experimentally, i.e. contact plasticity and then generalized plasticity as shown in Figure 3, are clearly distinguishable on the simulated curve. It should be noted that no serrations are present on the right part of the simulated curve, while this phenomenon appears experimentally from $\delta/D \approx 0.14$ (cf. Figure 3).

At microscopic scale, data resulting from the simulation can also be investigated by means of Figure 11, which presents the overall deformation map at stage 6, i.e. for a normalized displacement of $\delta/D \approx 0.08$. The simulated deformation is mainly concentrated in thin bands crossing the sample, proving that the compartmentalized model is able to reproduce the plasticity localization process. The resulting pattern clearly displays on the specimen surface the shapes in "χ" already observed on SEM micrographs as illustrated by Figures 4 and 5-f. The strain level in the center area of the sample is of the same order as the one measured by DIC and shown in Figures 6 and 7 at the same stage 7. The phenomenon of secondary SBs blocked by main SBs previously observed experimentally and illustrated by 5-f, -g and -h can also be observed in Figure 11. White arrows indicate three examples, among

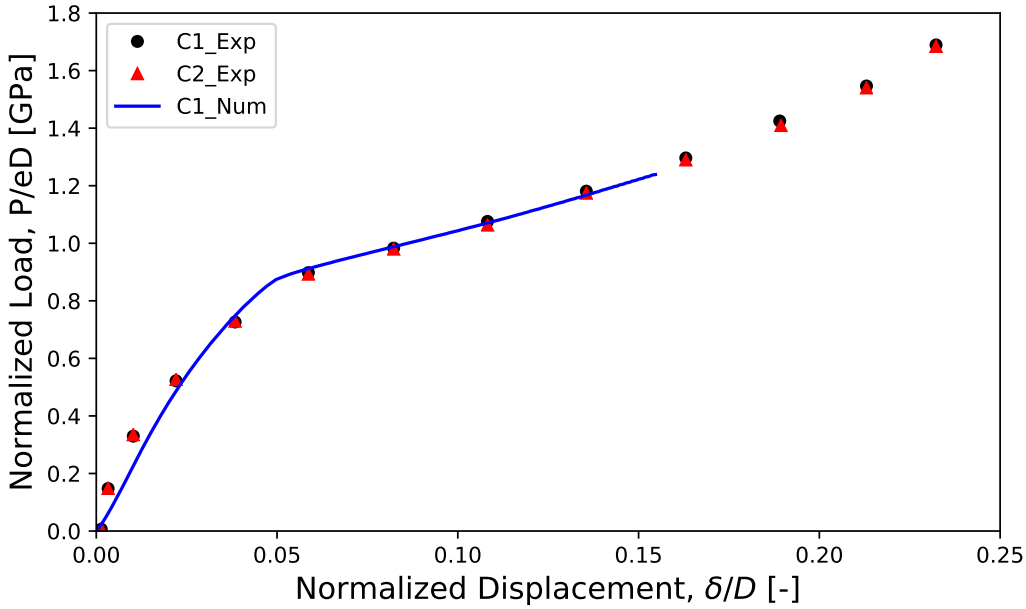

Figure 10. *Normalized load vs normalized displacement curves of the samples C1 and C2 compared with simulation results.*

many others, of a main SB that blocks secondary SBs. It is interesting to underline that such a simple model is able to capture this complex mechanism of interaction between and blockage of SBs.

Finally, Figure 12 presents experimental and numerical deformation maps of a common area, i.e. the sample C1 correlation zone, and at a common stage, i.e. the 7th stage corresponding to a normalized displacement of $\delta/D \approx 0.11$. The same data are also displayed as distribution histograms. Even if Figure 12 indicates that the SBs from the two data sets follow the same general pattern, clear discrepancies can also be observed. The higher peak of the experimental data distribution, as well as its thin and long right tail, clearly reveals that the simulated SBs are more diffuse and less intense than the experimental ones. Nevertheless, the mean values of the equivalent strain on the whole correlation zone are very similar: 0.099 and 0.109 for experimen-

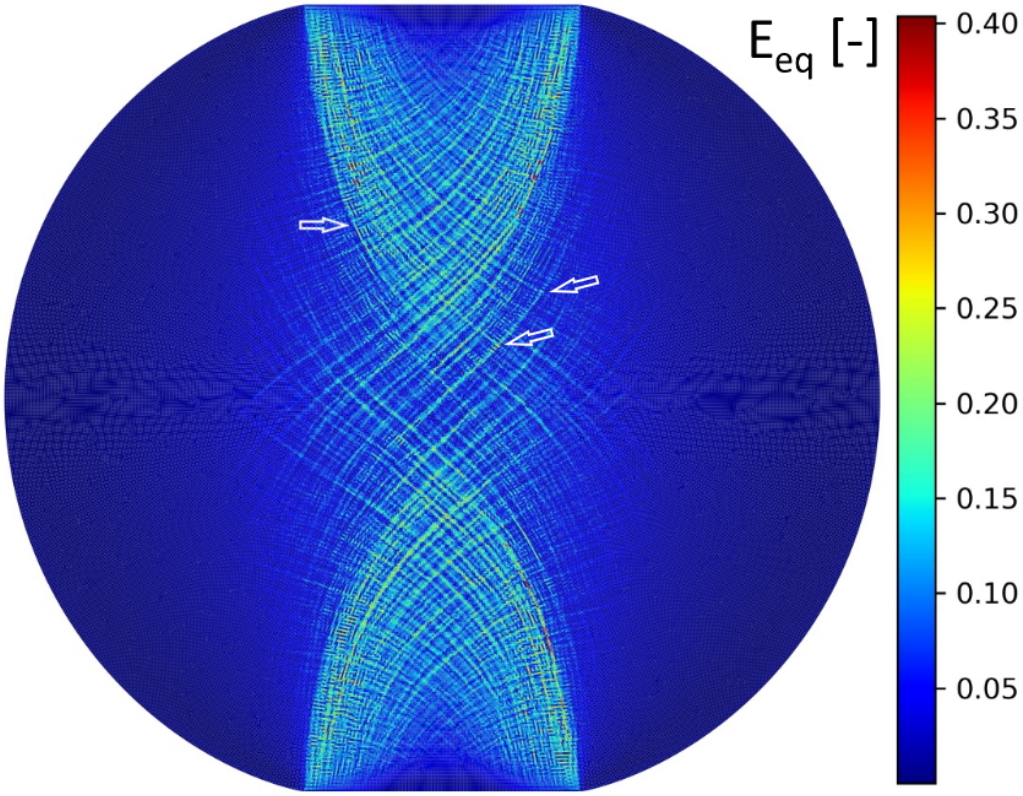

Figure 11. *Von Mises equivalent deformation maps of the sample obtained by simulation for a normalized displacement of* $\delta/D \approx 0.08$*, i.e. stage 6. The pattern appearing on the surface is very close to the shear band network observed experimentally and illustrated by Figures 4, 6 and 7. White arrows indicate three zones where secondary SBs are visibly blocked by a major SB*

tal and numerical results respectively. It is noteworthy that these results have been obtained without any tuning of the model parameters. It could be interesting to investigate in the future how changing the range of the random variable σ_y, or how changing its distribution function, can influence the morphology of the simulated SB network.

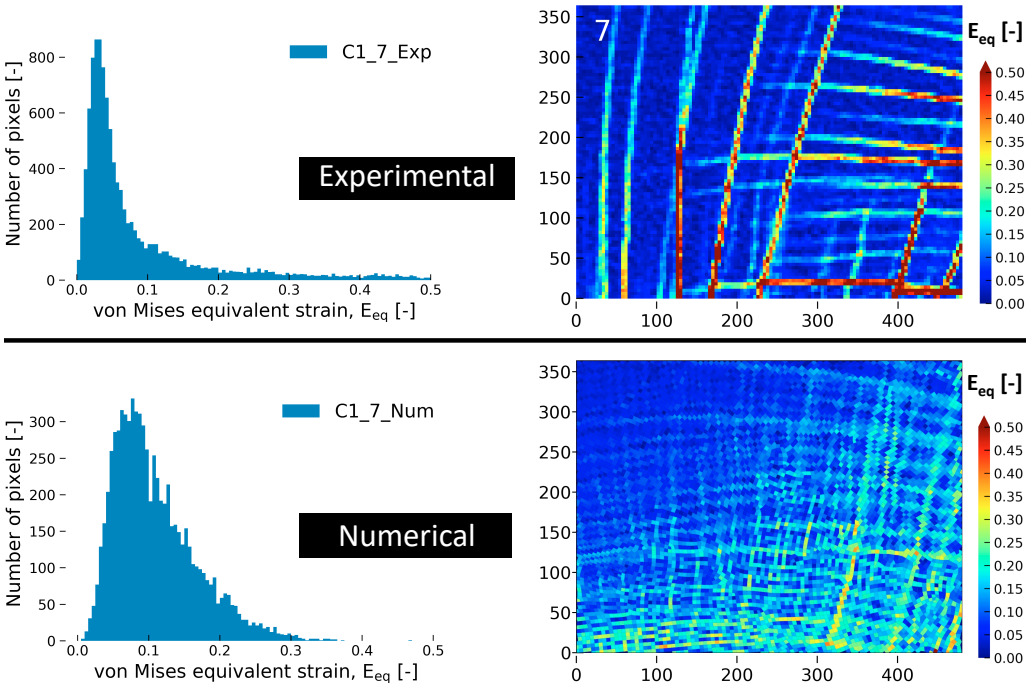

Figure 12. *Comparison between experimental (upper part) and numerical (lower part) values of the equivalent strain field in the same area (correlation zone of C1) and at the same stage of the test (7th stage). Results are represented in terms of statistical distribution (left) and spatial map (right).*

Although the compartmentalized model is based on a simple elastic-plastic law without hardening, its heterogeneous nature finally gives interesting results. At macroscopic scale, the load vs displacement curve obtained is very close to the experimental one and the overall SBs patterns are also very similar. Well-known models, such as the classic von Mises model or the pressure

sensitive Drucker-Prager model, have already proven that they can reproduce this overall behavior in BMGs [23], but they cannot induce localization. At local scale, phenomena such as the localization of plasticity in thin SBs and mutual interaction between these SBs are qualitatively reproduced by the compartmentalized model. Physically based softening models, such as Anand and Su [38] or Free Volume [45] models, are also able to reproduce the localization of the plastic flow in BMGs, but they are complex, i.e. depending on many parameters. Being rate-dependent, these models are less sensitive to the mesh size than rate-dependent models. Yet, under quasi-static conditions it remains mesh-sensitive (only under dynamic conditions is a length scale introduced). As a consequence, the compartmentalized model can be considered here as an intermediate way, between softening models and strain hardening models, to simulate BMG behavior at both scales. However, a finer tuning of its only parameter, the yield stresses σ_y, by optimizing its statistic distribution, could also result in better agreement at microscopic scale.

5. Concluding remarks

The high plastic deformation of a $Zr_{55}Cu_{30}Al_{10}Ni_5$ bulk metallic glass has been investigated by combining three experimental techniques: Brazilian tests, SEM microscopy and DIC analysis. Several results can be underlined:

- The diametral compression test (also called Brazilian test) has been shown to be a powerful experimental technique to induce and investigate high plasticity in BMGs. It has exhibited very good reproducibility in terms of load vs displacement response and the SBs always tend to draw a similar overall pattern. The plane face of the specimen that stays

visible during the test allows direct observation of steadily developing SBs.

- An innovative experimental technique associating the Brazilian test, SEM microscopy and DIC analysis and allowing the measurement of the strain field on a specimen surface with a 5 μm/pixel resolution during the test has been created. Extraordinarily high values of equivalent strain have been measured in SBs, up to 6 in the center of the sample. Such high values, directly obtained from deformation maps stemming from DIC analysis, have not already been reported in the literature, to our knowledge.

- The compartmentalized model, an original heterogeneous finite element model based on a simple constitutive law but randomly distributed in the mesh, has been used to describe the material behavior in a numerical simulation of the Brazilian test. Good agreement with the experiment has been shown at macroscopic scale in terms of load vs displacement response.

- At local scale, the strain field simulated has shown significant discrepancies with the experiment in terms of density and intensity of the SBs. However, this simple model provides a promising means of numerically reproducing the overall SB pattern, as well as the interlocking mechanism between major and secondary SBs observed experimentally.

It is noteworthy that in the present work only one set of parameters has been used for the compartmentalized model. After appropriate tuning, this model could potentially produce SB patterns much more similar to experi-

mental ones and offer better quantitative results at local scale. This will be the purpose of future work.

Data availability

Data will be made available on request.

Acknowledgements

We would like to thank E. Héripré and V. Doquet who made possible the in-situ compression tests and the DIC analysis of the resulting SEM images at the Laboratoire de Mécanique des Solides (École Polytechnique, Palaiseau) as well as M. Bornert (École des Ponts ParisTech) for his explanations on the software CorrelManuV. The authors are also grateful to S. Ruellan and P. Perron for specimen machining. This work has been supported by the French Ministry of Higher Education, Research and Innovation (Ph.D. grant for Sovannara Hin: Grant No. 2345-2012).

References

[1] C. Schuh, T. Hufnagel, U. Ramamurty, Mechanical behavior of amorphous alloys, Acta Mater. 55 (2007) 4067–4109.

[2] J. Xu, U. Ramamurty, E. Ma, The fracture toughness of bulk metallic glasses, JOM 62 (2010) 10–18.

[3] A. Greer, Y. Cheng, E. Ma, Shear bands in metallic glasses, Mater. Sci. Eng., R 74 (2013) 71–132.

[4] Z. F. Zhang, H. Zhang, X. F. Pan, J. Das, J. Eckert, Effect of aspect ratio on the compressive deformation and fracture behaviour of Zr-based bulk metallic glass, Philosophical Magazine Letters 85 (2005) 513–521.

[5] C. Bernard, V. Keryvin, V. Doquet, S. Hin, Y. Yokoyama, A sequential pre-cracking procedure to measure the mode-I fracture toughness of ultra pure bulk metallic glasses, Scr. Mater. 141 (2017) 58–61.

[6] S. Chen, J. Wang, L. Xia, Y. Wu, Deformation behavior of bulk metallic glasses and high entropy alloys under complex stress fields: A review, Entropy 2019, Vol. 21, Page 54 21 (2019) 54.

[7] S. Hin, C. Bernard, V. Doquet, Y. Yokoyama, A. Magueresse, V. Keryvin, Influence of as-cast spherulites on the fracture toughness of a Zr55Cu30Al10Ni5 bulk metallic glass, Materials Science and Engineering: A 740-741 (2019) 137–147.

[8] C. Bernard, V. Keryvin, Crystalline defects in bulk metallic glasses: consequences on fracture toughness determination and ductility, Journal of Physics: Condensed Matter 32 (2020) 483001.

[9] B. Sarac, J. Schroers, Designing tensile ductility in metallic glasses, Nature Communications 4 (2013) 2158.

[10] H. Choi-Yim, R. Busch, U. Köster, W. Johnson, Synthesis and characterization of particulate reinforced Zr57Nb5Al10Cu15.4Ni12.6 bulk metallic glass composites, Acta Mater. 47 (1999) 2455–2462.

[11] Z. Chu, G. Yuan, H. Kato, G. Xie, D. Yan, The effect of size and volume fraction of the reinforcement on mechanical property and deformation mechanism of the bulk metallic glassy composite, Journal of Alloys and Compounds 644 (2015) 25–29.

[12] S. Scudino, B. Jerliu, S. Pauly, K. Surreddi, U. Kühn, J. Eckert, Ductile bulk metallic glasses produced through designed heterogeneities, Scripta Mater. 65 (2011) 815–818.

[13] J. Dong, M. Gao, Y. Huan, Y. Feng, W. Liu, W. Wang, Enhanced tensile plasticity of Zr based bulk metallic glasses by a stress induced large scale flow, J. Alloys Compd. 727 (2017) 297–303.

[14] Y. Zhang, W. H. Wang, A. L. Greer, Making metallic glasses plastic by control of residual stress, Nature Materials 5 (2006) 857–860.

[15] S. H. Chen, T. Li, W. J. Chang, H. D. Yang, J. C. Zhang, H. H. Tang, S. D. Feng, F. F. Wu, Y. C. Wu, On the formation of shear bands in a metallic glass under tailored complex stress fields, Journal of Materials Science and Technology 53 (2020) 112–117.

[16] Y. Yokoyama, K. Yamano, K. Fukaura, H. Sunada, A. Inoue, Ductility improvement of

Zr55Cu30Al10Ni5 bulk amorphous alloy, Scripta Mater. 44 (2001) 1529–1533.

[17] L. He, M. Zhong, Z. Han, Q. Zhao, F. Jiang, J. Sun, Orientation effect of pre-introduced shear bands in a bulk-metallic glass on its "work-ductilising", Mater. Sci. Eng., A 496 (2008) 285–290.

[18] H. Yu, J. Hu, X. Xia, B. Sun, X. Li, W. Wang, H. Bai, Stress-induced structural inhomogeneity and plasticity of bulk metallic glasses, Scripta Mater. 61 (2009) 640–643.

[19] V. Keryvin, Indentation of bulk metallic glasses: Relationships between shear bands observed around the prints and hardness, Acta Mater. 55 (2007) 2565–2578.

[20] V. Keryvin, Indentation as a probe for pressure sensitivity of metallic glasses., J. Phys. Condens. Matter 20 (2008) 114119.

[21] M. Mellor, I. Hawkes, Measurement of tensile strength by diametral compression of discs and annuli, Engineering Geology 5 (1971) 173–225.

[22] Y. Wu, H. Bei, Y. Wang, Z. Lu, E. George, Y. Gao, Deformation-induced spatiotemporal fluctuation, evolution and localization of strain fields in a bulk metallic glass, International Journal of Plasticity 71 (2015) 136–145.

[23] J. Brest, V. Keryvin, P. Longère, Y. Yokoyama, Insight into plasticity mechanisms in metallic glasses by means of a Brazilian test and numerical simulation, Journal of Alloys and Compounds 586 (2014) S236–S241.

[24] Y. Yokoyama, Development of an Automatic Fabrication System for Cast Glassy Alloys, Metall. Mater. Trans. B Process Metall. Mater. Process. Sci. 46 (2015) 893–905.

[25] V. Keryvin, R. Crosnier, R. Laniel, V. H. Hoang, J.-C. Sangleboeuf, Indentation and scratching mechanisms of a ZrCuAlNi bulk metallic glass, J. Phys. D. Appl. Phys. 41 (2008) 074029.

[26] V. Keryvin, T. Rouxel, M. Huger, L. Charleux, Elastic moduli of a ZrCuAlNi bulk metallic glass from room temperature to complete crystallisation by in situ pulse-echo ultrasonic echography, J. Ceram. Soc. Japan 116 (2008) 851–854.

[27] L. Allais, M. Bornert, T. Bretheau, D. Caldemaison, Experimental characterization of the local strain field in a heterogeneous elastoplastic material, Acta Metallurgica et Materialia 42 (1994) 3865–3880.

[28] N. Lenoir, M. Bornert, J. Desrues, P. Bésuelle, G. Viggiani, Volumetric Digital Image Correlation Applied to X-ray Microtomography Images from Triaxial Compression Tests

on Argillaceous Rock, Strain 43 (2007) 193–205.

[29] P. Doumalin, M. Bornert, Micromechanical Applications of Digital Image Correlation Techniques, Springer Berlin Heidelberg, Berlin, Heidelberg, 2011. URL: http://link.springer.com/10.1007/978-3-642-57323-1_9. doi:10.1007/978-3-642-57323-1_9.

[30] V. Keryvin, X. Vu, V. Hoang, J. Shen, On the deformation morphology of bulk metallic glasses underneath a Vickers indentation, Journal of Alloys and Compounds 504 (2010) S41–S44.

[31] J. J. Lewandowski, A. L. Greer, Temperature rise at shear bands in metallic glasses, Nature Materials 5 (2006) 15–18.

[32] C. Su, L. Anand, Plane strain indentation of a Zr-based metallic glass: Experiments and numerical simulation, Acta Materialia 54 (2006) 179–189.

[33] L. Y. Chen, Q. Ge, S. Qu, Q. K. Jiang, X. P. Nie, J. Z. Jiang, Achieving large macroscopic compressive plastic deformation and work-hardening-like behavior in a monolithic bulk metallic glass by tailoring stress distribution, Applied Physics Letters 92 (2008).

[34] D. Wang, B. Sun, X. Niu, Y. Yang, W. Wang, C. Liu, Mutual interaction of shear bands in metallic glasses, Intermetallics 85 (2017) 48–53.

[35] K. Mondal, K. Hono, Geometry Constrained Plasticity of Bulk Metallic Glass, Materials Transactions 50 (2009) 152–157.

[36] J. X. Zhao, F. F. Wu, R. T. Qu, S. X. Li, Z. F. Zhang, Plastic deformability of metallic glass by artificial macroscopic notches, Acta Materialia 58 (2010) 5420–5432.

[37] V. Nekouie, S. Doak, A. Roy, U. Kühn, V. Silberschmidt, Experimental studies of shear bands in Zr-Cu metallic glass, Journal of Non-Crystalline Solids 484 (2018) 40–48.

[38] L. Anand, C. Su, A theory for amorphous viscoplastic materials undergoing finite deformations, with application to metallic glasses, J. Mech. Phys. Solids 53 (2005) 1362–1396.

[39] L. Bizet, L. Charleux, P. Balland, L. Tabourot, Influence of heterogeneities introduced into the modelling of a ring compression test, Archives of Civil and Mechanical Engineering 17 (2017) 365–374.

[40] L. Charleux, L. Tabourot, E. Roux, M. Issack Farah, L. Bizet, I. Farah, L. Bizet, Dependency of the Young's modulus to plastic strain in DP steels: A consequence of hetero-

geneity?, Materials Today Communications 24 (2020) 100972.

[41] L. Charleux, E. Roux, Compmod2: Compartmentalized Models with Argiope, 2019. Original-date: 2019-05-13T12:27:00Z.

[42] L. Charleux, E. Roux, C. Bernard, argiope, 2019. Original-date: 2016-06-16T12:03:27Z.

[43] L. Charleux, E. Roux, Dependency of the Young's modulus to plastic strain in DP steels: A consequence of heterogeneity?, 2019. Original-date: 2019-05-13T12:27:00Z.

[44] C. Geuzaine, J.-F. Remacle, Gmsh: A 3-D finite element mesh generator with built-in pre- and post-processing facilities, International Journal for Numerical Methods in Engineering 79 (2009) 1309–1331.

[45] F. Spaepen, A microscopic mechanism for steady state inhomogeneous flow in metallic glasses, Acta Metallurgica 25 (1977) 407–415.